

Colloidal structure, energy extensivity and Monte Carlo sampling properties of improved short-range interaction models for surfactant-coated magnetic nanoparticles

Aimê Gomes da Mata Kanzaki^a, Tiago de Sousa Araújo Cassiano^a, João Valeriano^b, Fabio Luis de Oliveira Paula^a, Leonardo Luiz e Castro^a

^aUniversidade de Brasília, Instituto de Física, Campus Universitário Darcy Ribeiro, Brasília, 70.910-900, DF, BR

^bAix-Marseille Université, CINAM, Turing Centre for Living Systems, Marseille, FR

Abstract

The standard DLVO theory offers a limited description of ionic-surfacted magnetic colloids in near aggregation regimes. Correcting the electrical double layer term for ionic surfactants is not enough to successfully simulate the systems. The correction of the van der Waals energy divergence at short interparticle distances is fundamental for proper Monte Carlo sampling of nanoparticles' configurations. We compare different short-range interaction models and show that a more detailed model leads to Monte Carlo simulations that better match theoretical expectations. Studying the energy scaling with the number of particles, we observe a slight deviation from energy extensivity across all models, small but still detectable via Akaike's information criterion. The more detailed model predicts a strong effect of particle-size dispersity on the transition between overall attraction and repulsion. More precise modeling can significantly affect numerical predictions, in particular, the effect of particle-size dispersity on the spatial structure of colloids with high volume fraction. This emphasizes the importance of nailing down better models for describing complex colloidal dispersions.

Keywords: colloid, ferrofluid, van der Waals, cohesive energy, Born-Mayer repulsion, extensivity, Monte Carlo

1. Introduction

Colloids, alongside their ample occurrence in nature and everyday products, are routinely synthesized in new varieties aiming at multiple applications. In particular, ferrofluids (magnetic colloids), made of magnetic iron oxide nanoparticles, have garnered significant interest due to their role in novel technological, biomedical, and environmental applications [1, 2, 3, 4]. Examples include their use as contrast agents in magnetic resonance imaging [5, 6], as multifunctional agents in theranostics [7], as a vehicle for the administration of targeted drugs [8, 9], and in cancer treatments through magnetohyperthermia [10, 11, 12, 13, 14, 15]. Improved targeted therapies, accurate diagnoses, and other innovative biomedical devices can emerge by combining the magnetic response of ferrofluids with the tailored functionalization of nanoparticle surfaces, thereby opening new frontiers in the field of nanomedicine.

A major issue in nanotechnological biomedicine [16] is the biocompatibility of the synthetic materials, being necessary to carry out extensive studies to ensure that they are pharmacologically inert for incorporation into living systems. Ferrofluid-based biomedical applications impose strong constraints for practical use. The particles must be chemically atoxic and the applied field's magnitude and frequency must not be unrestrictedly high to as to harm the body. Also, the attraction between the nanoparticles must not cause extensive agglomeration. It is known that agglomeration might make body clearance difficult, making the substance remain in the body for an extended time. For drug-

delivery applications, the concentration of nanoparticles might result in local deposition, overdosing the tissue and leading to cell death [17, 18]. For instance, it was found that the cytotoxicity of hydroxyapatite nanoparticles increases with agglomeration [19]. Agglomeration-induced damages to DNA are reported for carbon nanotubes [20] and anatase/rutile TiO₂ nanoparticles [21]. Therefore, an appropriate description of agglomeration is an important feature of colloidal theories.

Modifications to particle properties, such as surface functionalization or the addition of surfactants, can also alter the interaction energy between the particles and thus the colloidal stability of the ferrofluid. The DLVO theory is the standard formalism to describe colloidal particle-particle interactions [22, 23, 24, 25, 26, 27, 28]. In its simplest form, it comprises two components [29]: the van der Waals and the electric double-layer interactions. In general, several approaches are available to describe them. The van der Waals contribution can be modeled using either a macroscopic or a microscopic picture [29]. For instance, the Lifshitz macroscopic theory treats the colloid as a continuum [30]. Another alternative is to ground the formalism in quantum-mechanical principles, as done by London [31]. Concerning the DLVO, the Hamaker approach is used, according to which the interactions are calculated between simplified geometric shapes, such as planes and spheres [32, 23].

However, the DLVO theory has its limitations. In the small-separation regime, the van der Waals interaction can diverge if not properly controlled, leading to nonphysical trapping regions in theoretical simulations. When two nanoparticles come too close, they snap together and become inseparable, forming an unrealistically strong binding. Consequently, this limitation leads to a poor description of agglomeration and complex formation. The con-

Correspondence: joao-pedro.valeriano-miranda@univ-amu.fr
(João Valeriano)

ventional workaround in is to implement a cutoff distance. Then, two neighboring nanoparticles closer than this limit have the same attractive energy. However, this approach also has its own flaws, as the threshold distance is an arbitrary parameter and may still enforce trapping regions. In this context, developing improved strategies is crucial for both theoretical and practical perspectives. A more detailed theory of colloids for small-separation regimes might deliver a better description of agglomeration mechanisms, potentially offering better insights into how to mitigate them.

To study different modeling approaches for short-separation interactions between nanoparticles, we rely on Monte Carlo simulations. Computational simulation methods, such as Monte Carlo and molecular dynamics have been used extensively to evaluate the effect of nanoparticle interactions on ferrofluid's properties [33], considering factors such as concentration [34], pH [35], ionic strength [36], surface charge [37], particle size [38], polymer architecture [39], external magnetic field [40, 41], and confinement (e.g. inside liposomes) [42].

This work was mainly focused on the influence of size dispersion and short-range interaction on the self-organization of nanoparticles in magnetic colloids. We compared the results of three interparticle interaction models, differing mostly in their short-distance descriptions, used in Monte Carlo simulations of this reference system. We took as our study case a system formed by a magnetic fluid based on tartrate-coated magnetite nanoparticles [43] that was synthesized by thermal coprecipitation and dispersed in water at $pH \sim 7$ and a NaCl concentration of 0.15 M (physiological conditions). The particle diameters were fitted into a log-normal distributed with modal diameter $D_0 = 7.17$ nm and dispersion $\sigma = 0.24$ (for the sake of comparison, we simulated the system with and without diameter polydispersity).

In Section 2 we introduce the three models, proposing different solutions for correcting the small-distance interaction energy. In Section 3 we describe the simulation methods for studying the ferrofluid system, and proceed with an analysis of the energy extensivity properties of the different models, having in mind that the finite range interactions could lead to nonlinear scaling of energy with system size. We proceed with the presentation of our main results in Section 4 followed by a final discussion and conclusion.

2. Models

Colloids are commonly modeled as an ensemble of N interacting nanoparticles in a dispersion medium. The balance between the particle interactions and eventual external agents dictates the macroscopic properties. In our case, the physical description of a colloid involves summing the van der Waals (U_{vdw}), electric (U_{edl}), steric (U_{ste}), and magnetic interactions (U_{mag}).

$$U = U_{vdw} + U_{edl} + U_{ste} + U_{mag}. \quad (1)$$

The three interaction models between the nanocolloidal particles differ in how the van der Waals and the electronic repulsion (EDL) interactions are described. All other interactions pertaining to the description of the ferrofluid remain the same regardless of the model.

First, consider the interactions that are common to all models. Let R_i and R_j be the radii of nanoparticles i and j positioned at

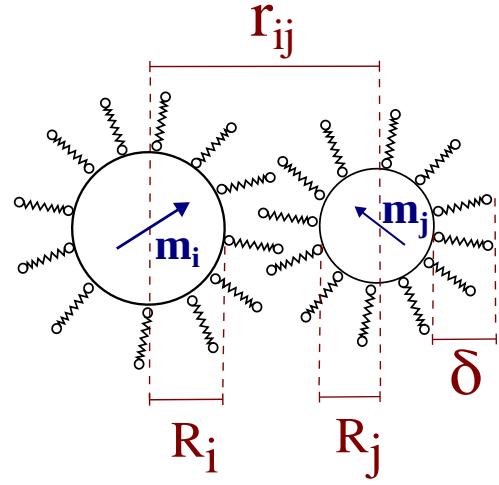


Figure 1: Illustration of pair of colloidal magnetic nanoparticles coated with surfactant molecules.

\vec{r}_i and \vec{r}_j , respectively. Then, $r_{ij} \equiv |\vec{r}_i - \vec{r}_j|$ is the corresponding center-to-center distance as illustrated in Figure 1. The magnetic moment of the i -th nanoparticle is

$$\vec{m}_i = MV_{mag(i)}\hat{u}_i, \quad (2)$$

where \hat{u}_i is the unit vector along the direction of the magnetic moment of the nanoparticle, M is the magnetization of the magnetite, and $V_{mag(i)}$ is the “magnetic volume” of the nanoparticle, given by

$$V_{mag(i)} = \frac{4\pi}{3}(R_i - \delta_s)^3, \quad (3)$$

in which δ_s is the length of its non-magnetic shell. Therefore, the dipolar interaction energy between the nanoparticles is expressed as

$$U_{mag}(r_{ij}, \vec{m}_i, \vec{m}_j) = \frac{\mu}{4\pi} \left[\frac{\vec{m}_i \cdot \vec{m}_j - 3(\vec{m}_i \cdot \hat{r}_{ij})(\vec{m}_j \cdot \hat{r}_{ij})}{r_{ij}^3} \right], \quad (4)$$

where μ is the magnetic permeability of the solvent.

The steric repulsion energy reads [44]

$$U_{ste}(r_{ij}) = \begin{cases} \frac{\pi\xi k_B T}{2} (2R_i)(2R_j) \left[2 - \frac{(r_{ij}-2R_j)}{\delta} - \frac{r_{ij}}{\delta} \ln \left(\frac{2(R_i+\delta)}{r_{ij}} \right) \right] & \text{for } r_{ij} < 2(R_{ij} + \delta), \\ 0 & \text{otherwise,} \end{cases} \quad (5)$$

in which ξ is the grafting parameter (surface density of the adsorbed molecules), δ is the length of the surfactant layers, and R_{ij} is the arithmetic mean of R_i and R_j ,

$$R_{ij} = \frac{R_i + R_j}{2}. \quad (6)$$

Let us now describe the interactions that differ across the models. The first model avoids the van der Waals divergence by limiting the separation distance to a predefined threshold (s_{min}). Any pairs whose surfaces are closer than this limit will have the same

energy as if the distance is s_{min} . The second model overcomes the divergence by considering the length of atomic bonds, effectively adjusting the separation distance in the energy expressions so that the divergence range is never reached. The third model involves replacing U_{vdw} , for small separations, with the cohesive energy combined with the Born-Mayer repulsion. We set $s_{min} = 0.01$ nm for the three models to compare the different approaches at small separations where the system transitions from a mesoscopic to a microscopic realm. This value is close to the Born-Mayer decay parameter $L = 0.03084$ nm, while still above the order of magnitude in which finer effects such as atomic bond vibrations become significant [45, 46].

2.1. Model 1

In the first model, the van der Waals energy value decreases as the surface-surface distance moves towards its minimum cutoff value of $s_{min} = 0.01$ nm, and then it is held constant for smaller distances ($s < s_{min}$).

The van der Waals energy between two particles R_i and R_j is written as [32]

$$U_{vdw}(r_{ij}) = -\frac{A}{6} \left[\frac{2R_i R_j}{r_{ij}^2 - (R_i + R_j)^2} + \frac{2R_i R_j}{r_{ij}^2 - (R_i - R_j)^2} + \ln \left(\frac{r_{ij}^2 - (R_i + R_j)^2}{r_{ij}^2 - (R_i - R_j)^2} \right) \right] \quad (7)$$

The value of s_{min} was set as 0.01 nm, leading to a deep well in the van der Waals energy, as shown in Figure 2a. The chosen s_{min} is significantly lower than the conventional use of van der Waals interactions. We recall that the cutoff distance is a form of mitigating the energy divergence for small-range separations. Therefore, the value of s_{min} is, within a physical range, arbitrary and often tuned to avoid sampling problems. Here, we opted for a lower s_{min} to showcase the effect of the corrections proposed in the work via Models 2 and 3.

The electrostatic repulsion is described using the linear superposition model [47], adapted to the fact that the surface charge is at the surfactant layer extremity:

$$U_{edl}(r_{ij}) = 4\pi k_B T (2\rho_{ion}) \lambda_D \left[R_i^* \Psi_{(R_i^*)} \right] \left[R_j^* \Psi_{(R_j^*)} \right] \times \exp \left(-\frac{r_{ij} - R_i^* - R_j^*}{\lambda_D} \right) / r_{ij}, \quad (8)$$

where the function $\Psi_{(R)}$ is expressed as

$$\Psi_{(R)} = 4 \tanh \left(\frac{e\psi_{(R)}}{4k_B T} \right), \quad (9)$$

(from the two-flat-plane model via the Derjaguin approximation for two spheres) ensuring that U_{edl} closely approximates the most accurate models for both small and large separations, and

$$R^* = R + \delta \quad (10)$$

is the effective nanoparticle radius adjusted by δ , the thickness of the surfactant layer (the length of the molecules), k_B is the Boltzmann constant, T is the absolute temperature, e is the elementary charge, $\psi_{(R)}$ is the value of the electric potential on the surface of a nanoparticle of radius R (R_i or R_j in Eq. 9), s_σ is the distance

between the charged surfaces, and λ_D is the Debye length, given by

$$\lambda_D = \left(\frac{\epsilon k_B T}{(2\rho_{ion}) z_{ion}^2 e^2} \right)^{1/2}, \quad (11)$$

where ϵ is the electrical permittivity of the solvent, ρ_{ion} is the ion concentration of the solvent, and z_{ion} is the valence of the ions in the solution. The system simulated in this study has a 1:1 electrolyte (NaCl), therefore we used $z_{ion} = 1$.

The value of $\psi_{(R)}$ is calculated as [48]

$$\psi_{(R)} = \frac{k_B T}{ze} \operatorname{acosh} \left(\frac{\sigma_{(R)}^2}{4\epsilon \rho_{ion} k_B T} \right), \quad (12)$$

where $\sigma_{(R)}$ is the surface charge density of a nanoparticle of radius R , calculated through the relation [43]

$$\sigma_{(R)} = \left[ze \left(\frac{R}{R + \delta} \right)^2 \right] \xi, \quad (13)$$

which expresses the linear relation between the surface charge density and the surfactant density (ξ), considering that each surfactant molecule contributes with a charge ze at its extremity, located at a distance δ from the nanoparticle surface. Note that $\psi_{(R)}$ carries a dependence on particle size via the surface charge density, consistent with the expected behavior of the electric potential under changes in particle size.

Note that the accuracy of the Derjaguin approximation is higher for small separation-to-diameter ratios. However, for larger distances, the interaction becomes progressively smaller, lowering its importance in the overall energy balance. Therefore, for the sake of simplicity, the same expression is applied for other separation distances since its importance is reduced. This represents the standard approach in simulating colloids within the DLVO formalism. Specifically, the EDL interaction, as present here, is the usual approach to model charge surface interactions in colloid models, extensively applied in the past to represent interactions in the same class of colloids [49, 50]. Model 1, described in this subsection, will be a reference for comparison with two other strategies, Models 2 and 3, described next. Importantly, Model 3 will specifically address the limitation in the description of the EDL interaction by introducing a new expression, derived via the Schnitzer–Morozov technique [51], which extends the validity of the Derjaguin approximation into the long-range regime.

2.2. Model 2

The second model considers the length of a typical atomic bond in the nanoparticle bulk (L_B) and prevents the divergence of the van der Waals energy by adding to the intersurface distance of the colloidal particle pairs, which is equivalent to changing the center-to-center distance as in

$$r_{ij} \rightarrow r_{ij} + L_B. \quad (14)$$

Incorporating this distance into the center-to-center separation aims to preserve the qualitative characteristics of the interaction curve, with noticeable deviations emerging only at distances near L_B , where the divergence occurs (Figure 2b). This procedure is similar to a modification tested by White [52] for the

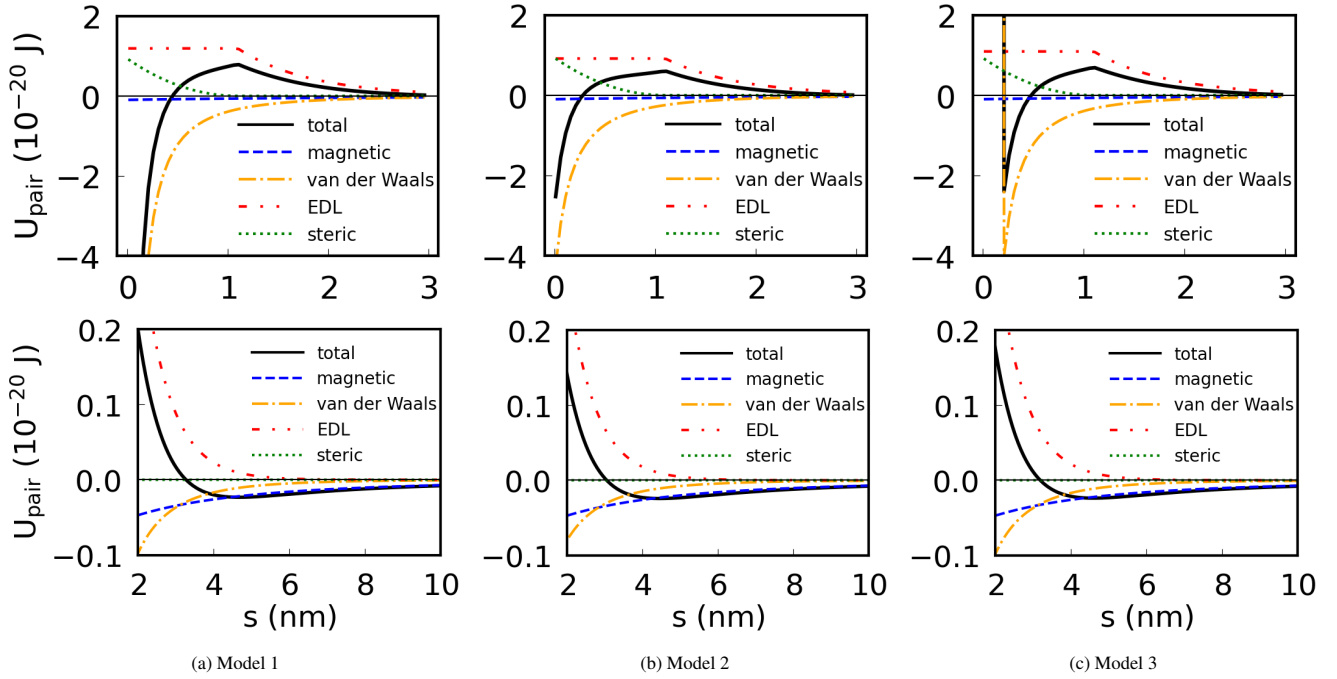


Figure 2: Total energy of a nanoparticle pair (U_{pair}), according to each model, as a function of the distance between their surfaces ($s \equiv s_{ij} = r_{ij} - 2R_{ij}$). The two particles are identical, with radii $R_i = R_j = 3.585$ nm ($= D_0/2$), disposed with magnetic dipoles aligned in a head-to-tail fashion (note the negative sign of the magnetic contribution). Other parameters are set as given in Appendix A. The graphs in the top row show small distances (and consequently high energy values). In contrast, the graphs in the bottom row show the corresponding curves at larger distances (and low energy), evidencing the long-range nature of magnetic interactions. Models 2 and 3 have different strategies to deal with the divergence of the van der Waals energy, while it is barely treated in Model 1.

van der Waals interaction between planes. We have chosen the value of a typical atomic bond distance of the maghemite bulk, $L_B = 0.19$ nm, estimated for a Fe–O bond [53, 54].

Thus, the van der Waals energy between the nanoparticles i and j is then written as

$$U_{vdw}(r_{ij}) = -\frac{A}{6} \left[\frac{2R_i R_j}{(r_{ij} + L_B)^2 - (R_i + R_j)^2} + \frac{2R_i R_j}{(r_{ij} + L_B)^2 - (R_i - R_j)^2} + \ln \left(\frac{(r_{ij} + L_B)^2 - (R_i + R_j)^2}{(r_{ij} + L_B)^2 - (R_i - R_j)^2} \right) \right]. \quad (15)$$

For the sake of consistency, the same modification is applied to the EDL interaction:

$$U_{edl}(r_{ij}) = \frac{4\pi k_B T (2\rho_{ion}) \lambda_D}{r_{ij} + L_B} \left[4R_i^* \tanh \left(\frac{e\psi_{(R_i)}}{4k_B T} \right) \right] \left[4R_j^* \tanh \left(\frac{e\psi_{(R_j)}}{4k_B T} \right) \right] \times \exp \left(-\frac{r_{ij} + L_B - R_i^* - R_j^*}{\lambda_D} \right). \quad (16)$$

The values of $\psi_{(R_i)}$ (and $\psi_{(R_j)}$) are given by Eq. 12, as in Model 1.

2.3. Model 3

Another approach consists of replacing, for small separations, the van der Waals energy with the Born-Mayer repulsion and the cohesive energy [55], so that the expression for the joint expression looks like

$$U_{vdw-bm}(r_{ij}) = \begin{cases} U_{vdw}(r_{ij}) & \text{if } r_{ij} > R_{ij} + L_B, \\ U_{vdw}(L_B) + U_{coh}(r_{ij}) + U_{bm}(r_{ij}) & \text{otherwise,} \end{cases} \quad (17)$$

where $U_{vdw}(L_B)$ is the value of $U_{vdw}(r_{ij})$ for $r_{ij} = L_B$ (value shown in Appendix A), U_{bm} is the energy related to the Born-Mayer repulsion [56], given by

$$U_{bm} = A_{bm} \exp \left(-\frac{r_{ij} - R_{ij}}{L_{bm}} \right), \quad (18)$$

and

$$U_{coh} = A_{int} W_{coh}, \quad (19)$$

where A_{int} is the area between the spheres in which their surfaces are close enough to form atomic bonds (details of the calculation were shown in a previous article [55]) and W_{coh} is the cohesion work (value shown in Appendix A).

The authors also propose a change in the electrostatic interaction energy that makes it accurate at all distances, using a technique introduced by Schnitzer and Morozov [51]. The resulting expression is

$$U_{edl-sm}(r_{ij}) = -4\pi k_B T (2\rho_{ion}) \lambda_D \left[4R_i^* \tanh \left(\frac{e\psi_i}{4k_B T} \right) \right] \left[4R_j^* \tanh \left(\frac{e\psi_j}{4k_B T} \right) \right] \times e^{(R_i+R_j)/\lambda_D} Ei \left(-\frac{r_{ij} - 2\delta}{\lambda_D} \right), \quad (20)$$

where ρ_{ion} is the concentration of ions in the solvent, ψ_i and ψ_j are the electrical potential values on the surfaces of the spheres, Ei is the exponential integral function, and λ_D is the Debye length.

The energy curves of Model 3 are depicted in Figure 2c. Although the energy curves provided by the three models are very similar for long distances (bottom row of Figure 2), they exhibit significant differences for short distances (top row) in terms of

shape and minimum value. Therefore, the models represent the colloid using distinct physical descriptions that we shall compare in the results of this study.

3. Simulation

The system was studied using Monte Carlo simulations, through an adaptation of the Metropolis-Hastings algorithm. Each simulation starts with a random configuration and small changes in the particle positions and orientations are made in successive steps. A newly generated configuration is accepted whenever the system energy decreases. If the energy increases by ΔE , the new configuration is accepted with a probability proportional to $\exp(-\beta\Delta E)$, with $\beta = (k_B T)^{-1}$. The scale of such changes is dynamically adjusted such that 50% of the generated configurations are accepted, by following the algorithm rules. After every 50 000 steps, the program calculates how much the ever-reached minimum value of total energy has decreased: sampling begins when this variation is less than 0.05, continues for at least other 50 000 steps, and finishes when the variation is less than 0.005. Those parameters are summarized in [Appendix A](#). The quantities of interest are averaged over the sampling steps of at least ten independent simulations with each set of physical parameters.

To represent a sample from a macroscopic object, we simulated the colloids using periodic boundary conditions with a minimum image. The pair interactions between two particles are calculated over the smallest distance between them, considering their images through the periodic boundaries. Also, the periodic boundary conditions are used at the Monte Carlo steps: When generating a new sample configuration, the nanoparticles' positions are weakly shifted. If the shift moves the particle crosses the boundaries of the original box, it is reinserted near the opposite face of the box, according to the periodic conditions.

Initially, we assess the total energy extensivity of the three models. Given the finite range of pair interactions, we can expect some deviation from a linear scaling of energy with system size (increasing the number of particles and the volume of the system while preserving the volume fraction of particles). It is easy to see that if we split a colloidal system with a plane separating it into parts A and B, the total energy U will not be just the sum of the energies of the separate parts, $U_A + U_B$. There can be a significant contribution to the total energy that is associated with pairs of particles near the separating plane, with each particle of the pair on a different side. To evaluate this contribution, we simulated the colloidal solution with increasingly higher particle numbers and evaluated their corresponding energies. The particle concentration was kept constant at 5 % (volume fraction ϕ), a relatively high value that forces more particles into small separations. The interactions between the nanoparticles are higher in this regime, allowing a better evaluation of the system deviation from extensivity. After that, we simulated the ferrofluid at a lower concentration of $\phi = 0.47\%$, which was investigated in detail in our experimental reference [43]. The simulations included some variations as a means of comparing the effects of the characteristics and conditions of the colloid: monodisperse and polydisperse diameter distributions; non-magnetic and magnetic particles; and zero and finite applied magnetic fields. The monodisperse system corresponds to a log-normal distribution with a dispersion parameter of zero ($\sigma_R = 0$), meaning that all diameters are equal to the

Table 1: Average first neighbor distance $\langle s_1 \rangle$ for monodisperse and polydisperse systems, at a volume fraction of 5% simulated through different models, with standard errors. The short-range repulsions of Model 3 caused overall higher values, especially for the monodisperse system (in contrast with the other models, with higher distances for the polydisperse system).

Model	Average first neighbor distance (nm)	
	monodisperse	polydisperse
1	2.17 ± 0.04	2.61 ± 0.04
2	2.06 ± 0.05	2.57 ± 0.05
3	3.12 ± 0.06	2.74 ± 0.04

median diameter of the polydisperse system. All results presented in the next section are based on averages took over 10 separate Monte Carlo simulations, to account for the random aspect of these simulations. Other parameters are shown in [Appendix A](#).

4. Results

Dispersity differentially affects colloidal structure depending on short-range interaction models. We start characterizing the magnetic colloids under the three models by looking into the average first neighbor distance $\langle s_1 \rangle$ for a volume fraction $\phi = 5\%$ (see Table 1; the dependence of $\langle s_1 \rangle$ with the number of particles is shown in the Supplementary Figure S1).

Model 1 and Model 2 lead to first neighbor distances that are larger polydisperse than in the monodisperse scenario. This is due to the EDL repulsion increasing faster than the magnetic dipolar and van der Waals attractions, for increasing diameters in the short range. The log-normal distribution is skewed towards larger diameters, which favors higher barriers that prevent nanoparticles from reaching the primary energy minima (see Supplementary Figure S2).

Model 3 resulted in more sparsely distributed nanoparticles, a consequence of the short-range repulsions. However, in contrast with the other models, the values of $\langle s_1 \rangle$ are now larger for the monodisperse system. This can be understood by looking into the position of the secondary energy minima, which move to shorter distances and become deeper due to the increased magnetic attraction of larger particles (see Supplementary Figure S3). This moving to shorter distances and deepening of the secondary energy minimum is still observed for pairs of particles with different sizes, as one increases the radius of either particle in a pair (Supplementary Figure S4).

We also analyzed $\langle s_1 \rangle$ for the ferrofluid at the lower volume fraction of 0.47%, which characterizes the real sample [43]. We considered both non-magnetic and magnetic colloids, with and without an external magnetic field (Table 2 for monodisperse and Table 3 for polydisperse scenarios). For this decreased volume fraction, the average first-neighbor distance is larger (compare to Table 1), and small-range repulsions included in Model 3 are only relevant for a minority of the nanoparticles. The differences between the $\langle s_1 \rangle$ values for non-magnetic and magnetic colloids at zero field, and magnetic colloids at 1 T are not significant, considering the uncertainties. Our focus is on the nanoparticle interactions, more easily studied in the magnetic colloid at zero field.

We also compare Models 2 and 3 by looking into how they change the system compared to Model 1, which is an established formalism in colloid simulations. Both Models 2 and 3 predict

Table 2: Average first neighbor distance $\langle s_1 \rangle$ for the monodisperse systems simulated through different models, with standard errors, at a volume fraction of 0.47% [43]. The values given by Model 3 are slightly higher, with a more significant disagreement with the other models, considering the standard errors.

Model	Average first neighbor distance (nm)		
	non-magn.	magnetic $B = 0$ T	magnetic $B = 1$ T
1	11.88 ± 0.07	12.24 ± 0.98	12.11 ± 0.09
2	11.80 ± 0.08	11.94 ± 0.17	12.24 ± 0.92
3	12.45 ± 0.55	12.37 ± 0.75	12.34 ± 0.87

Table 3: Average first neighbor distance $\langle s_1 \rangle$ for the polydisperse system simulated through different models, with standard errors. The differences between the values are negligible, except for the slightly higher values of Model 3 for the non-magnetic system. This is explained by the larger particles that increase the EDL repulsion, which, in magnetic colloids, is counterbalanced by the increase of the magnetic dipolar attraction.

Model	Average first neighbor distance (nm)		
	non-magn.	magnetic $B = 0$ T	magnetic $B = 1$ T
1	13.31 ± 0.12	13.47 ± 0.12	13.42 ± 0.11
2	13.50 ± 0.13	13.20 ± 0.13	13.44 ± 0.11
3	13.61 ± 0.09	13.76 ± 0.13	13.75 ± 0.09

equilibrium distances smaller than those predicted by Model 1 (Supplementary Figure S5). For pairs of particles with fixed radii sum $R_i + R_j$, the distinctions between Model 1 and both Models 2 and 3 are more pronounced in the monodisperse scenario ($R_i = R_j$). This is true for both the position and the energy level of the secondary equilibrium. The difference between Models 1 and 2 in the position of the secondary equilibrium presents a higher variability over particles' radii combinations, while Model 3 differs from Model 1 through a more systematic and better-conserved shift. Compared to Model 1, both Models 1 and 3 lead to increased energy depths, indicating an improved description of agglomeration mechanisms. The stronger secondary minimum may serve as a competing factor in the formation of strongly bound nanoparticles that were artificially trapped in the first minimum in Model 1.

Models 2 and 3 improve Monte Carlo sampling of the system. Going into more detail of the colloidal structure, we look into the pair correlation function $g(r)$ (Figures 3a for mono and 3b polydisperse systems in the zero field condition). As expected, the peak heights are proportional to the energy well depths (Figure 2), with Models 1 and 2 resulting in higher peaks and Model 3 in lower ones. The polydisperse systems pair-correlation functions exhibit more dispersed peaks, as a result of the statistical variability of the nanoparticle diameters, making multiple separation distances available depending on the radii of particles in a pair. However, it is important to note that the number and position of these multiple peaks can be sensitive to fluctuations in the Monte Carlo simulations.

The interaction between magnetic particles depends on their positions and orientations, as defined by their magnetic moment dipoles. Thus, we also computed the angular pair correlation function $g(r, \theta)$ (Figure 4). In direct correspondence to the radial pair correlation function $g(r)$ (Figure 3), brighter regions indicate a higher probability of encountering a pair of particles sep-

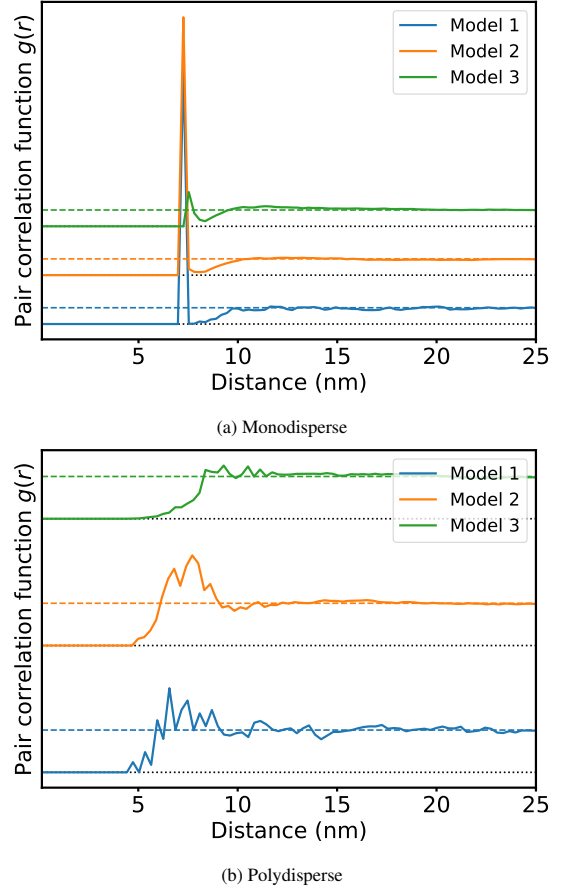


Figure 3: Pair correlation function for the mono and polydisperse systems in the zero field condition, simulated through the three models, averaged over 10 simulations. Higher peaks are observed for Models 1 and 2, and the lowest ones with Model 3. Diameter polydispersity makes the peaks more dispersed. The curves in different colors are shifted vertically for easier comparison, with the dotted lines corresponding to the 0 particle baseline, and the colored dashed curves corresponding to the large distance limit $g(r) \rightarrow 1$.

arated by a distance r at an angle θ relative to the z -axis. The darker regions at the centers appear because r is the distance between the centers of two particles, and the nanoparticles are hard spheres whose volumes do not overlap. The yellow ring between $r = 5$ and $r = 10$ for the monodisperse systems is associated with the first neighbor distance, bounded from below by the particle diameter. For polydisperse systems, the minimum distance between two particles' centers can vary significantly therefore, we no longer have such a characteristic first-neighbor-distance ring.

There is a prominent contrast among $g(r, \theta)$ plots of different models. For both poly and monodisperse solutions, the heatmaps from Models 2 and 3 are significantly smoother than those from Model 1. The bright spots in Model 1 (Figures 4a and 4d) are the result of diverging attractive short-range interactions that trap pairs of nanoparticles in their interaction potential wells. This can also be seen in the tail of the $g(r)$ curves in Figure 3, although more discreetly due to the averaging over dipole orientations.

The highly negative energy values that arise for pairs of particles in Model 1 cause a generally reduced mobility of the particles in the Monte Carlo simulation. When there are interactions with different orders of magnitude, the algorithm prioritizes changes in nanoparticles that most affect the dominant interaction, the di-

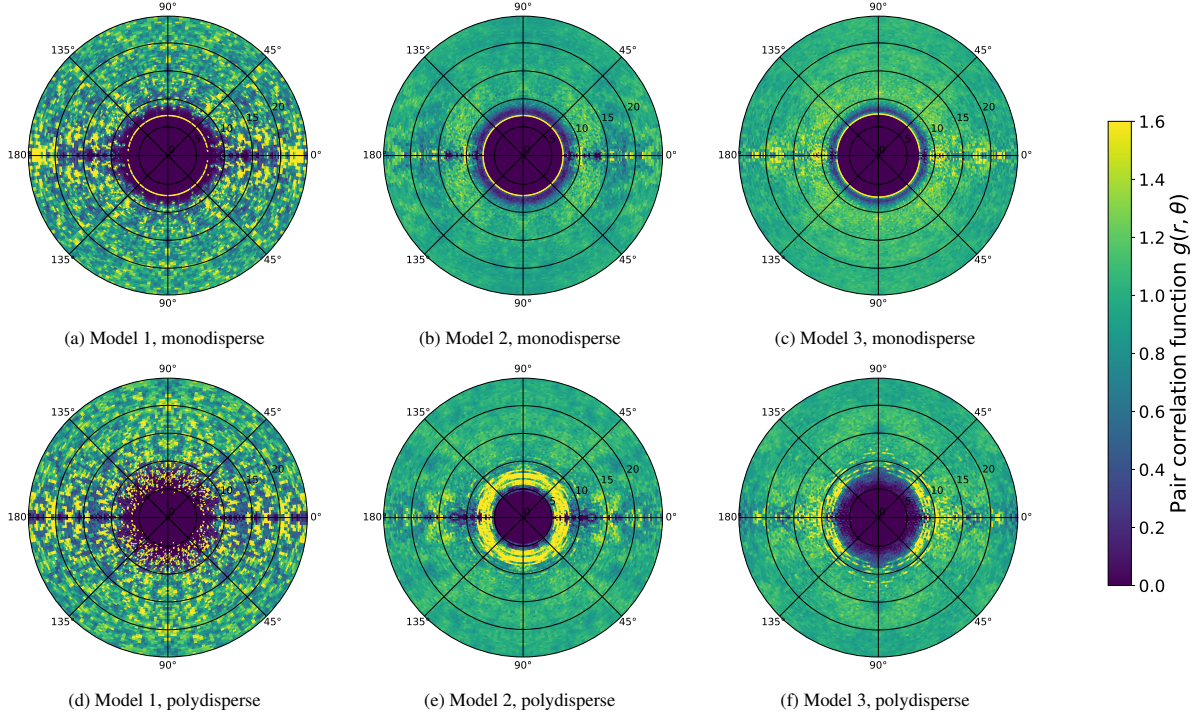


Figure 4: **Models 2 and 3 improve Monte Carlo sampling of the system.** Pair correlation function $g(r, \theta)$, simulated through the three models, for magnetic systems at zero applied field condition, averaged over 10 simulations. Volume fraction of $\phi = 0.47\%$. r is in units of nanometers. The horizontal axis ($\theta = 0^\circ$) in the heatmaps coincides with the z -axis of a coordinate system xyz . The spots observed for Model 1 are caused by particle pairs trapped in local minima or the deep well as two surfaces approach each other. The dispersal of the first-neighbor-distance ring in the bottom row highlights the influence of polydispersity on the magnetic structure. For improved visualization, the colormap is limited to 1.6, and all points with $g(r, \theta) > 1.6$ are shown in the same color.

verging van der Waals attraction. As a result, the total energy reaches a deep local minimum (see also the difference of orders of magnitude between the energies of different models in Figure 5). The remaining components lose part of their influence in determining the colloidal stationary configuration. Consequently, finding the global minimum becomes numerically challenging, as changes in the non-dominant interactions produce negligible effects on the total energy. In other words, when the interaction energy between a particle pair is too negative, other particles may also “freeze” in energetically unfavorable configurations.

The heatmaps for Models 2 and 3 do not have such prominent spots, presenting only barely discernible lighter regions near the central ring. For Model 2, this result is attributed to the higher EDL repulsion involving larger colloidal particles, which prevents configuration freezing, thus allowing particles to move towards the main minimum of pair interactions.

For Model 3, adopting the Born-Mayer repulsion and the cohesive energy for small separations avoids the implicit assumptions of the van der Waals energy expressions, which commonly do not apply near the microscopic scale. Besides this physical motivation that can provide some trust in these corrections used in Model 3, this model also presents better Monte Carlo sampling properties. Overall, this leads to a higher level of confidence in the results obtained from Model 3.

Our results show that an inadequate application of energy models lead to an unexpected behavior of the simulation algorithm. This can lead to a dramatic bias when estimating physical properties of the system, in particular to the study of agglomeration effects in colloids. Relying on a simplified pair energy function may result in a poor description of the agglomeration mechanism.

In contrast, using a more refined approach could not only offer a better representation but also more accurately identify the conditions that lead to these states.

Magnetic colloids weakly deviate from energy extensivity across all models. For the three short-range interaction models, we investigate the energy scaling with the total number of particles in simulations (Figure 5). The energy variation is fit assuming that, for each number N of particles, the energy likelihood follows a normal distribution with fixed N -dependent variance σ_N^2 and mean given by either a linear model $U_1(N) = aN$ or a quadratic one $U_2(N) = bN + cN^2$. Fitting parameters were obtained via maximum likelihood estimation, solved through a weighted linear regression. Weights were given by the inverses of energies’ variances over simulations with the same N . We use the implementation of the weighted least squares solver by the Python library statsmodels [57].

Computing the Akaike information criterion (AIC) [58, 59] for the linear and quadratic models, we obtain smaller values for the quadratic model $U_2(N)$ in all cases. Therefore, the quadratic model provides a better description of the energy scaling with the number of particles. We do not claim that the true energy scaling is quadratic with the number of particles, though it could be expected given the pairwise nature of interactions. We merely state that our result shows that the energy scaling is nonlinear, as expected given the long range of interactions.

Notice that the difference in AIC scores is the smallest for Model 3 in the polydisperse case (Fig. 5f), given the stronger fluctuation in energy when compared to other models. The enhanced fluctuations reduce the statistical power to identify the contribution of the second-order term, but also indicate higher

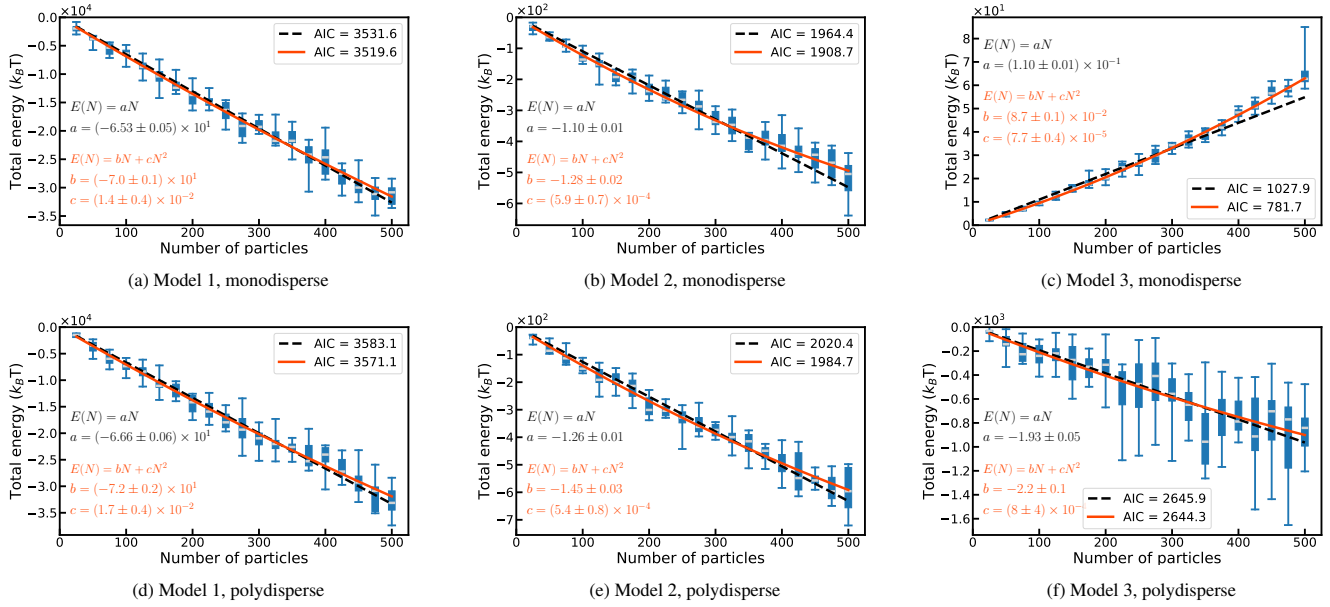


Figure 5: Magnetic colloids weakly deviate from energy extensivity across all models. For each model, simulations are done at a volume fraction of 5%. In the polydisperse scenario, the median radius is $R_0 = 3.585$ nm, with a log-normal distribution with dispersion $\sigma_R = 0.12$. In the boxplots, the boxes represent the interquartile ranges and the whiskers include the total range of samples, with the grey lines indicating the median values. The black dashed lines show a linear fit of the total energy to particle number, and the solid orange lines show a quadratic fit, in both cases with the intercept set to zero. In all cases, the AIC is smaller for the quadratic fit, confirming the presence of a non-extensive contribution to the energy, albeit relatively small, given estimated values for the parameter c in the quadratic fits.

freedom to reach more diverse configurations with this energy model. Model 3 also contrasts with the other models for giving a positive total energy value for the monodisperse system (Fig. 5c), indicating an overall repulsion between the nanoparticles, a clear consequence of the Born-Mayer interaction. However, for the polydisperse scenario, the total energy is negative as in the other cases, a consequence of the higher magnetic dipolar and van der Waals attractions between the large particles that are present in the polydisperse colloids.

Interestingly, the ratio between the mean values of coefficients c and b is the highest for Model 3 (about an order of magnitude larger than for Models 1 and 2), leading to the largest difference in AIC scores for the monodisperse case. In this regime, the system is near the threshold between the globally repulsive (with overall positive interaction energy) and globally attractive (negative energy) regimes, enhancing the importance of the second-order term cN^2 – notice the smaller energy scale in Figure 5c.

5. Discussion

In summary, we studied three models (Model 1, 2, 3) aimed to simulate magnetic colloids in aggregation regimes. Model 1 represents the standard approach, rooted in the DLVO theory, which served as reference. Model 2 and 3 correspond to proposed corrections in the van der Waals and electric repulsion interactions at the small-range regime.

Our analysis revealed that better short-range interaction models can significantly change predictions about the effect of particle-size dispersity on the colloidal structure. Importantly, the more realistic Model 3 predicts that, at high volume fraction ($\phi = 5\%$), size polydispersity should decrease the average first

neighbor distance $\langle s_1 \rangle$, opposite to what is expected from Models 1 and 2. This difference could provide an interesting direction for future experimental research. Experimentally identifying more realistic models for describing magnetic colloids could significantly impact the development of the field. It would allow for more trustworthy theoretical predictions about costly and hard-to-perform experiments, such as studying magnetic colloids in complex environments.

Moreover, improving short-range interaction models also aids convergence of Monte Carlo simulations by reducing sampling biases. The main problem with the standard DLVO theory, characterized here by Model 1, is the divergence of the van der Waals energy to negative infinity as the distance between the surfaces of two particles tends to zero. This divergence dramatically hampers the Monte Carlo sampling of the system, as seen in the salt and pepper patterns in the heatmaps for Model 1 in Figure 4. This happens due to van der Waals energy contribution that leads to deep energy wells at very short distances. Consequently, many particle pairs fall into these local minima, unrealistically reducing the overall mobility of particles during the simulations.

We provided two different models that solve the energy divergence, improving Monte Carlo sampling compared to the conventional DLVO approach [22, 23, 24, 25, 26, 27, 28]. In particular, Model 3 is more realistic from a theoretical point of view, as it substitutes the van der Waals attraction with the cohesive energy and the Born-Mayer repulsion at short distances. We argue that Model 3 might have better sampling properties than Model 2: For all 3 models, the secondary energy minimum moves to smaller distances as we shift from monodisperse to polydisperse samples (Supplementary Figures S3 and S4). However, we only see a decrease in the average first neighbor distance $\langle s_1 \rangle$ due to poly-

dispersity in simulations of Model 3. This could be an indication of better sampling properties of Model 3 compared to Model 2. We still need experimental data to confirm the correctness of this prediction, as mentioned above.

As long-range interactions can lead to non-extensive energies, we investigated the change in total energy with the number of particles for a high-density ferrofluid solution, and its variation across models. The results showed a slight shift from linearity for all models studied, confirmed by the AIC scores of linear and nonlinear models of energy scaling with the number of particles. The nonlinearity was more pronounced for Model 3 in monodisperse configuration. This is a borderline case between the globally repulsive and attractive regimes, leading to smaller absolute energy values. Provided experimental validation, the models can be useful for precise identification of ideal ideal particle size to maintain the necessary colloidal structure of different applications.

Supporting Information

Supplementary files associated with this article can be found in the online version.

Acknowledgements

The authors gratefully acknowledge financial support from Fundação de Apoio à Pesquisa do Distrito Federal (FAPDF) through Grant No. 00193-00001713/2024-10.

Appendix A. Parameters

Table A.4: Metropolis-Hasting algorithm parameters.

Variable	Description	Value
$N_{MC[max]}$	maximum number of MC steps	300 000
$N_{MC[chk]}$	number of MC steps between convergence checks	50 000
ΔU_{ini}	energy variation to begin sampling	0.05
ΔU_{fin}	energy variation to finish sampling	0.005
α	target acceptance rate in Metropolis algorithm	0.5
s_{min}	surface minimum distance	0.01 nm
N	number of particles in the box	25 (minimum) 500 (maximum) [43]

Table A.5: Dispersed phase: magnetite nanoparticles.

Parameters	Description	Value
D_0	median diameter	7.17 nm
R_0	median radius	3.585 nm [43]
σ_D	diameter dispersion	0.24
σ_R	radius dispersion	0.24 [43]
M	magnetization	$4.71 \times 10^5 \text{ A m}^{-1}$ [43]
ξ	grafting parameter	$2.0 \times 10^{17} \text{ m}^{-2}$ [43]
δ	surfactant layer length	0.55 nm [43]
δ_s	excluded radius	0.8 nm
W_{coh}	cohesive energy (maghemite)	1.38 J m^{-2} [60]
L_B	atomic bond distance (maghemite Fe–O)	0.19 nm [53, 54]
A_{bm}	Born-Mayer parameter A	1207.6 eV [56]
L_{bm}	Born-Mayer parameter L	0.3084 Å [56]
λ_D	Debye length	1.1 nm [43]

Table A.6: Dispersion medium: water.

Parameters	Description	Value
μ	magnetic permeability	$1.26 \times 10^{-6} \text{ H m}^{-1}$
ρ_{ion}	ion concentration	0.15 mol L ⁻¹ [43]

Table A.7: System's parameters.

Parameters	Description	Value
ϕ	volume fraction	0.05 (5 %) 0.0047 (0.47 %) [43]
T	temperature	300 K [43]
A	Hamaker constant	$0.40 \times 10^{-21} \text{ J}$ [43]

References

- [1] R. L. Bailey, “Lesser known applications of ferrofluids,” *Journal of Magnetism and Magnetic Materials*, vol. 39, p. 178, 1983.
- [2] K. Raj and R. Moskowitz, “Commercial applications of ferrofluids,” *Journal of Magnetism and Magnetic Materials*, vol. 85, no. 1, pp. 233–245, 1990.
- [3] J. Roger, J. N. Pons, R. Massart, A. Halbreich, and J. C. Bacri, “Some biomedical applications of ferrofluids,” *The European Physical Journal - Applied Physics*, vol. 5, no. 3, pp. 321–325, 1999.
- [4] C. Scherer and A. M. Figueiredo, Neto, “Ferrofluids: properties and applications,” *Brazilian Journal of Physics*, vol. 35, no. 3A, p. 718, 2005.

- [5] G. Song, M. Kenney, Y. S. Chen, X. Zheng, Y. Deng, Z. Chen, S. X. Wang, S. S. Gambhir, H. Dai, and J. Rao, "Feco/graphitic-shell nanocrystals as advanced magnetic-resonance-imaging and near-infrared agents," *Nat. Mater.*, vol. 5, pp. 971–976, 2006.
- [6] M. G. Harisinghani, J. Barentsz, P. F. Hahn, W. M. Dersno, S. Tabatabaei, C. H. van de Kaa, J. de la Rosette, and R. Weissleder, "Noninvasive detection of clinically occult lymph-node metastases in prostate cancer," *N. Engl. J. Med.*, vol. 348, pp. 2491–2499, June 2003.
- [7] G. Song, M. Kenney, Y. Chen, X. Zheng, Y. Deng, Z. Chen, S. Wang, S. Gambhir, H. Dai, and J. Rao, "Carbon-coated feco nanoparticles as sensitive magnetic-particle-imaging tracers with photothermal and magnetothermal properties," *Nat Biomed Eng.*, vol. 4, no. 3, 2020.
- [8] C. Alexiou, R. Schmid, R. Jurgons, C. Bergemann, W. Arnold, and F. G. Parak, "Targeted tumor therapy with magnetic drug targeting," in *Ferrofluids: magnetically controllable fluids and their applications*, pp. 233–251, Ed. Stefan Odenbach, 2002.
- [9] U. Maver, M. Bele, D. Makovec, S. Čampelj, J. Jamnik, and M. Gaberšček, "Incorporation and release of drug into/from superparamagnetic iron oxide nanoparticles," *Journal of Magnetism and Magnetic Materials*, vol. 321, no. 19, pp. 3187–3192, 2009.
- [10] M. Sato, T. Yamashita, M. Ohkura, Y. Osai, A. Sato, T. Takada, H. Matsusaka, I. Ono, Y. Tamura, N. Sato, Y. Sasaki, A. Ito, H. Honda, K. Wakamatsu, S. Ito, and K. Jimbow, "N-propionyl-cysteaminyphenol-magnetite conjugate (nprcap/m) is a nanoparticle for the targeted growth suppression of melanoma cells," *Journal of Investigative Dermatology*, vol. 129, no. 9, pp. 2233–2241, 2009.
- [11] E. L. Verde, G. T. Landi, J. A. Gomes, M. H. Sousa, and A. F. Bakuzis, "Magnetic hyperthermia investigation of cobalt ferrite nanoparticles: Comparison between experiment, linear response theory, and dynamic hysteresis simulations," *J. Appl. Phys.*, vol. 111, p. 123902, June 2012.
- [12] M. Santos Carrião and A. Bakuzis, "Mean-field and linear regime approach to magnetic hyperthermia of core-shell nanoparticles," *Nanoscale*, vol. 8, pp. 8363–8377, 2016.
- [13] G. N. Rego, J. B. Mamani, T. K. Souza, M. P. Nucci, H. R. Silva, and L. F. Gamarra, "Therapeutic evaluation of magnetic hyperthermia using fe3o4-aminosilane-coated iron oxide nanoparticles in glioblastoma animal model," *Einstein (São Paulo)*, vol. 17, no. 4, p. eAO4786, 2019.
- [14] M. S. Gopika, B. B. Lahiri, B. Anju, J. Philip, and S. S. Pillai, "Magnetic hyperthermia studies in magnetite ferrofluids based on bio-friendly oils extracted from calophyllum inophyllum, brassica juncea, ricinus communis and madhuca longifolia," *Journal of Magnetism and Magnetic Materials*, vol. 537, p. 168134, 2021.
- [15] E.-A. Moacă, V. Socoliuc, D. Stoian, C. Watz, D. Flondor, C. Păcurariu, R. Ianoș, C. I. Rus, L. Barbu-Tudoran, A. Semenescu, *et al.*, "Synthesis and characterization of bioactive magnetic nanoparticles from the perspective of hyperthermia applications," *Magnetochemistry*, vol. 8, no. 11, p. 145, 2022.
- [16] Y. Patil-Sen, "Advances in nano-biomaterials and their applications in biomedicine," *Emerging Topics in Life Sciences*, vol. 5, no. 1, pp. 169–176, 2021.
- [17] A. Bruinink, J. Wang, and P. Wick, "Effect of particle agglomeration in nanotoxicology," *Archives of toxicology*, vol. 89, pp. 659–675, 2015.
- [18] M. Epple, "Review of potential health risks associated with nanoscopic calcium phosphate," *Acta biomaterialia*, vol. 77, pp. 1–14, 2018.
- [19] L. Andrée, L. S. Joziassse, M. J. Adjobo-Hermans, F. Yang, R. Wang, and S. C. Leeuwenburgh, "Effect of hydroxyapatite nanoparticle crystallinity and colloidal stability on cytotoxicity," *ACS Biomaterials Science & Engineering*, vol. 10, no. 11, pp. 6964–6973, 2024.
- [20] P. Wick, P. Manser, L. K. Limbach, U. Dettlaff-Weglikowska, F. Krumeich, S. Roth, W. J. Stark, and A. Bruinink, "The degree and kind of agglomeration affect carbon nanotube cytotoxicity," *Toxicology letters*, vol. 168, no. 2, pp. 121–131, 2007.
- [21] Z. Magdolenova, D. Bilaničová, G. Pojana, L. M. Fjellsbø, A. Hudecova, K. Hasplova, A. Marcomini, and M. Dusinska, "Impact of agglomeration and different dispersions of titanium dioxide nanoparticles on the human related in vitro cytotoxicity and genotoxicity," *Journal of Environmental Monitoring*, vol. 14, no. 2, pp. 455–464, 2012.
- [22] N. Tufenkji and M. Elimelech, "Deviation from the classical colloid filtration theory in the presence of repulsive dlvo interactions," *Langmuir*, vol. 20, no. 25, pp. 10818–10828, 2004.
- [23] J. Israelachvili, *Intermolecular e surface forces*. Academic Press, 1992.
- [24] E. M. Hoek, S. Bhattacharjee, and M. Elimelech, "Effect of membrane surface roughness on colloid- membrane dlvo interactions," *Langmuir*, vol. 19, no. 11, pp. 4836–4847, 2003.
- [25] F. L. O. Paula, R. Aquino, G. J. da Silva, J. Depeyrot, F. A. Tourinho, J. O. Fossum, and K. D. Knudsen, "Small-angle X-ray and small-angle neutron scattering investigations of colloidal dispersions of magnetic nanoparticles and clay nanoplatelets," *Journal of Applied Crystallography*, vol. 40, pp. s269–s273, Apr 2007.
- [26] F. L. O. Paula, G. J. da Silva, R. Aquino, J. Depeyrot, J. O. Fossum, K. D. Knudsen, G. Helgesen, and F. A. Tourinho, "Gravitational and magnetic separation in self-assembled clay-ferrofluid nanocomposites," *Brazilian Journal of Physics*, vol. 39, pp. 163 – 170, 04 2009.

- [27] W. B. Russel, W. Russel, D. A. Saville, and W. R. Schowalter, *Colloidal dispersions*. Cambridge university press, 1991.
- [28] C. Shen, F. Wang, B. Li, Y. Jin, L.-P. Wang, and Y. Huang, "Application of dlvo energy map to evaluate interactions between spherical colloids and rough surfaces," *Langmuir*, vol. 28, no. 41, pp. 14681–14692, 2012.
- [29] Y. Liang, N. Hilal, P. Langston, and V. Starov, "Interaction forces between colloidal particles in liquid: Theory and experiment," *Advances in colloid and interface science*, vol. 134, pp. 151–166, 2007.
- [30] E. M. Lifshitz, M. Hamermesh, *et al.*, "The theory of molecular attractive forces between solids," in *Perspectives in theoretical physics*, pp. 329–349, Elsevier, 1992.
- [31] F. London, "Zur theorie und systematik der molekularkräfte," *Zeitschrift für Physik*, vol. 63, no. 3, pp. 245–279, 1930.
- [32] H. Hamaker, "The london—van der waals attraction between spherical particles," *Physica*, vol. 4, no. 10, pp. 1058–1072, 1937.
- [33] K. Ono, Y. Matsukawa, Y. Saito, H. Aoki, K. Era, T. Aoki, and T. Yamaguchi, "Monte carlo simulation for morphology of nanoparticles and particle size distributions: comparison of the cluster–cluster aggregation model with the sectional method," *Journal of Nanoparticle Research*, vol. 242, p. 242, 2015.
- [34] L. L. Castro, R. Miotto, and A. F. Bakuzis, "Concentration effects on the grafting of magnetic nanoparticles by Monte Carlo simulations," *Journal of Applied Physics*, vol. 99, no. 08S101, 2006.
- [35] F. L. O. Paula, L. L. Castro, T. S. A. Cassiano, S. G. dos Santos, G. Gomide, J. Depeyrot, and A. F. C. Campos, "pH-dependent phase transitions in ferrofluids: A monte carlo simulation study using an extended dlvo model," *Colloids and Surfaces A: Physicochemical and Engineering Aspects*, vol. 658, p. 130578, 2023.
- [36] G. Brancolini, V. M. Rotello, and S. Corni, "Role of ionic strength in the formation of stable supramolecular nanoparticle–protein conjugates for biosensing," *International Journal of Molecular Sciences*, vol. 23, no. 4, 2022.
- [37] A. F. C. Campos, E. P. Marinho, A. Ferreira, F. A. Tourinho, F. L. O. Paula, and J. Depeyrot, "X-dlvo interactions between nanocolloidal magnetic particles: The quantitative interpretation of the ph-dependent phase diagram of edl-mf," *Brazilian Journal of Physics*, vol. 39, pp. 230–235, 2009.
- [38] X. Deng, Z. Huang, W. Wang, and R. N. Davé, "Investigation of nanoparticle agglomerates properties using monte carlo simulations," *Advanced Powder Technology*, vol. 27, no. 5, pp. 1971–1979, 2016.
- [39] D. Mostarac, Y. Xiong, O. Gang, and S. Kantorovich, "Nanopolymers for magnetic applications: how to choose the architecture?," *Nanoscale*, vol. 14, no. 31, pp. 11139–11151, 2022.
- [40] G. Mériguet, M. Jardat, and P. Turq, "Structural properties of charge-stabilized ferrofluids under a magnetic field: A brownian dynamics study," *The Journal of chemical physics*, vol. 121, no. 12, pp. 6078–6085, 2004.
- [41] F. L. de Oliveira Paula, "Saxs analysis of magnetic field influence on magnetic nanoparticle clusters," *Condensed Matter*, vol. 4, no. 2, 2019.
- [42] M. A. Salvador, A. S. Costa, M. Gaeti, L. P. Mendes, E. M. Lima, A. F. Bakuzis, and R. Miotto, "Characterization, nanoparticle self-organization, and monte carlo simulation of magnetoliposomes," *Phys. Rev. E*, vol. 93, p. 022609, Feb 2016.
- [43] A. F. Bakuzis, L. C. Branquinho, L. L. e Castro, M. T. de Amaral e Eloí, and R. Miotto, "Chain formation and aging process in biocompatible polydisperse ferrofluids: Experimental investigation and monte carlo simulations," *Advances in Colloid and Interface Science*, vol. 191–192, pp. 1–21, 2013.
- [44] R. E. Rosensweig, *Ferrohydrodynamics*. Dover, 1997.
- [45] S. Konaka and M. Kimura, "On an empirical rule for the mean amplitudes of bonded atom pairs," *Journal of Molecular Spectroscopy*, vol. 36, no. 3, pp. 521–527, 1970.
- [46] T. Scheele and T. Neudecker, "On the interplay between force, temperature, and electric fields in the rupture process of mechanophores," *ChemPhysChem*, vol. 25, Sept. 2024.
- [47] W. B. Russel, D. A. Saville, and W. R. Schowalter, *Colloidal Dispersions*. Cambridge Monographs on Mechanics, Cambridge University Press, 1989.
- [48] R. J. Hunter, "Colloid science," in *Zeta Potential in Colloid Science* (R. H. Ottewill and R. L. Rowell, eds.), p. 386, Academic Press, 1981.
- [49] S. Kumar, C. Ravikumar, and R. Bandyopadhyaya, "State of dispersion of magnetic nanoparticles in an aqueous medium: experiments and monte carlo simulation," *Langmuir*, vol. 26, no. 23, pp. 18320–18330, 2010.
- [50] M. A. Salvador, A. S. Costa, M. Gaeti, L. P. Mendes, E. M. Lima, A. F. Bakuzis, and R. Miotto, "Characterization, nanoparticle self-organization, and monte carlo simulation of magnetoliposomes," *Physical review E*, vol. 93, no. 2, p. 022609, 2016.
- [51] O. Schnitzer and M. Morozov, "A generalized derjaguin approximation for electrical-double-layer interactions at arbitrary separations," *The Journal of Chemical Physics*, vol. 142, no. 24, p. 244102, 2015.
- [52] L. R. White, "van der waals interaction energy and disjoining pressure at small separation," *Journal of Colloid and Interface Science*, pp. 338–343, 2010.

- [53] M. L. Fdez-Gubieda, A. García-Prieto, J. Alonso, and C. Meneghini, *X-Ray Absorption Fine Structure Spectroscopy in Fe Oxides and Oxyhydroxides*, ch. 17, pp. 397–422. John Wiley & Sons, Ltd, 2016.
- [54] M. Coduri, P. Masala, L. Del Bianco, F. Spizzo, D. Ceresoli, C. Castellano, S. Cappelli, C. Oliva, S. Checchia, M. Allietta, D.-V. Szabo, S. Schlabach, M. Hagelstein, C. Ferrero, and M. Scavini, “Local structure and magnetism of Fe_2O_3 maghemite nanocrystals: The role of crystal dimension,” *Nanomaterials*, vol. 10, no. 5, 2020.
- [55] L. L. Castro, C. C. C. Amorin, P. V. Miranda, J. T. S. A. Cassiano, and F. L. O. Paula, “The role of small separation interactions in ferrofluid structure,” *Colloids and surfaces A*, vol. 635, no. 128082, 2022.
- [56] G. V. Lewis and C. R. A. Catlow, “Potential models for ionic oxides,” *Journal of Physics C: Solid State Physics*, vol. 18, pp. 1149–1161, 1985.
- [57] S. Seabold and J. Perktold, “statsmodels: Econometric and statistical modeling with python,” in *9th Python in Science Conference*, 2010.
- [58] H. Akaike, “A new look at the statistical model identification,” *IEEE Transactions on Automatic Control*, vol. 19, no. 6, pp. 716–723, 1974.
- [59] D. Anderson and K. Burnham, “Model selection and multi-model inference,” *Second. NY: Springer-Verlag*, vol. 63, no. 2020, p. 10, 2004.
- [60] I. I. Diakonov, “Thermodynamic properties of iron oxides and hydroxides. ii. estimation of the surface and bulk thermodynamic properties of ordered and disordered maghemite ($\gamma\text{-Fe}_2\text{O}_3$),” *European Journal of Mineralogy*, vol. 10, no. 1, pp. 17–30, 1998.

Electronic Supplementary Information for: Effects of diameter polydispersity and small-range interactions on the structure of biocompatible colloidal nanoparticles[†]

Aimê Gomes da Mata Kanzaki¹, Tiago de Sousa Araújo Cassiano¹, João Pedro Valeriano Miranda^{*,2}, Fabio Luis de Oliveira Paula¹, and Leonardo Luiz e Castro¹

¹ *University of Brasília, Instituto de Física, Campus Universitário Darcy Ribeiro, Brasília, 70.910-900, DF, BR*

² *Aix-Marseille Université, CINAM, Turing Centre for Living Systems, Marseille, FR*

^{*}joao-pedro.valeriano-miranda@univ-amu.fr

Dependence of average first-neighbor distance with the number of particles in the simulation

Figure S1 shows $\langle s_1 \rangle$ versus the number of particles inside the simulation box for Model 1 (a), Model 2 (b) and Model 3 (c). The particle concentration (volume fraction) is $\phi = 5\%$.

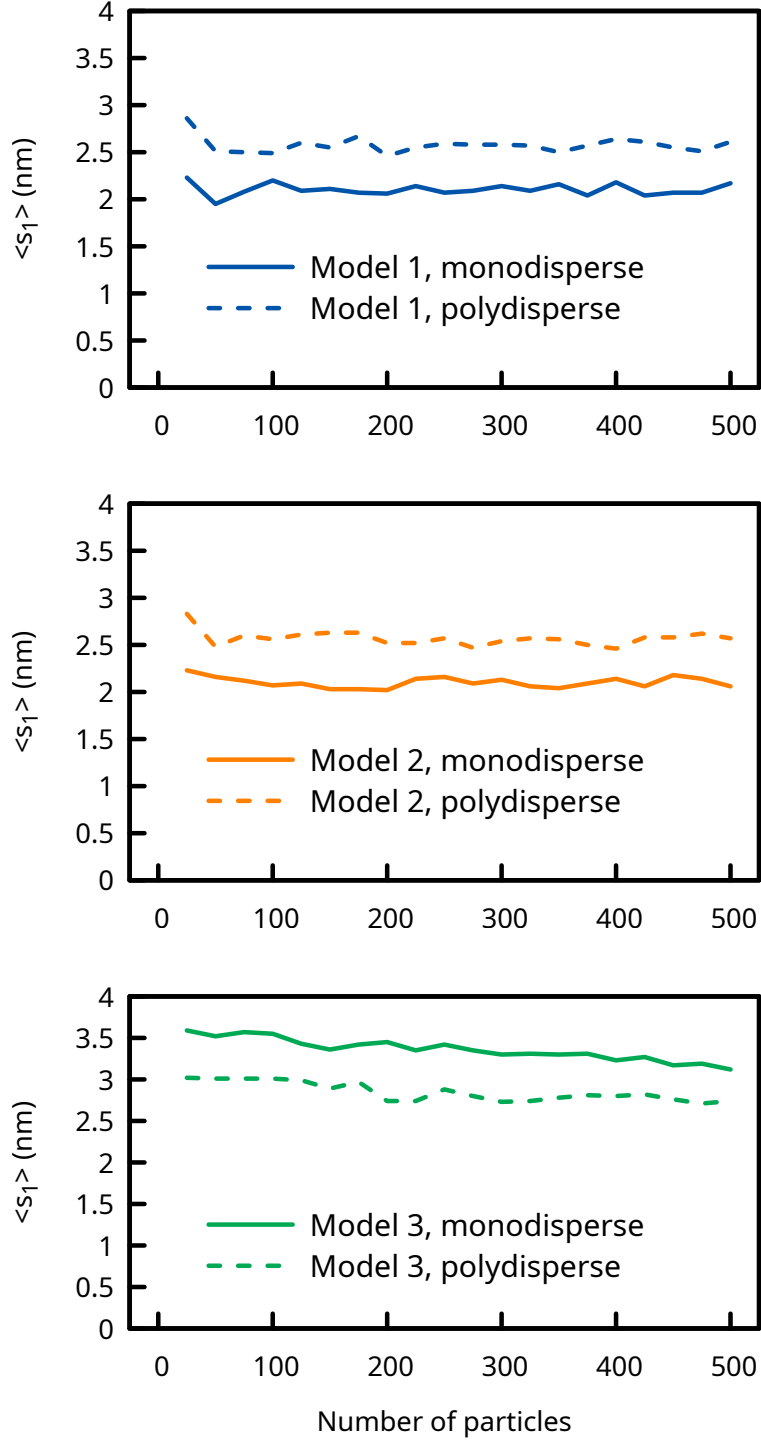


Figure S1: Average first-neighbor distance ($\langle s_1 \rangle$) versus number of simulated particles (N), for the system at a $\phi = 5\%$.

Interaction energy profiles from each model

The variation of the primary minimum radius depends on the particle radius only by a tiny margin, as one can conclude by comparing Figure S2. Thus, we made a deeper analysis of the secondary minimum, whose position and depth vary with the nanoparticle radii more significantly, as shown in Figure S3.

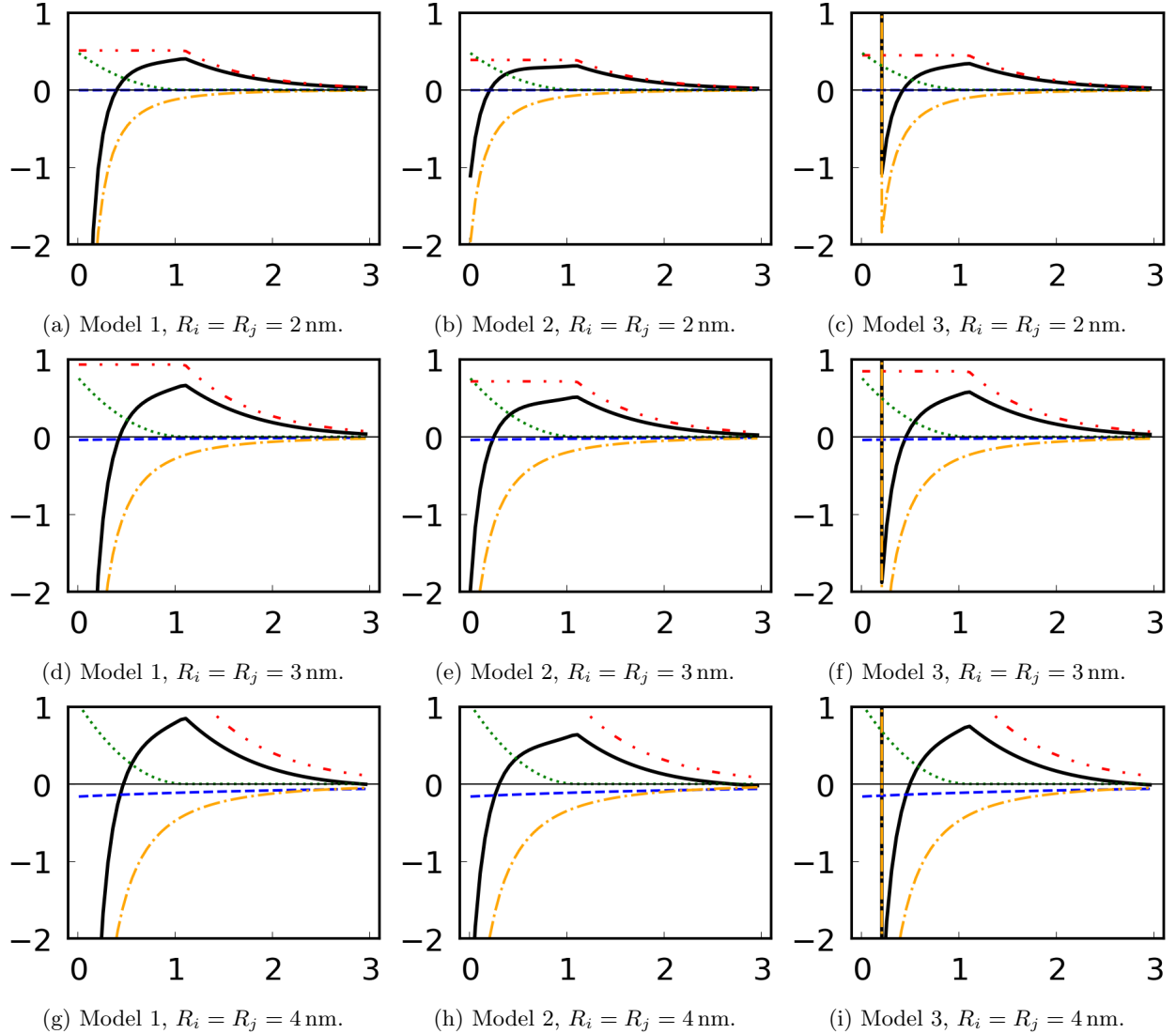


Figure S2: Interaction energy of two nanoparticles with equal radii in dependence on their intersurface distance, in the short range (0 nm to 3 nm), for the models 1, 2 and 3, from left to right. Other nanoparticle parameters are as shown in the article appendices.

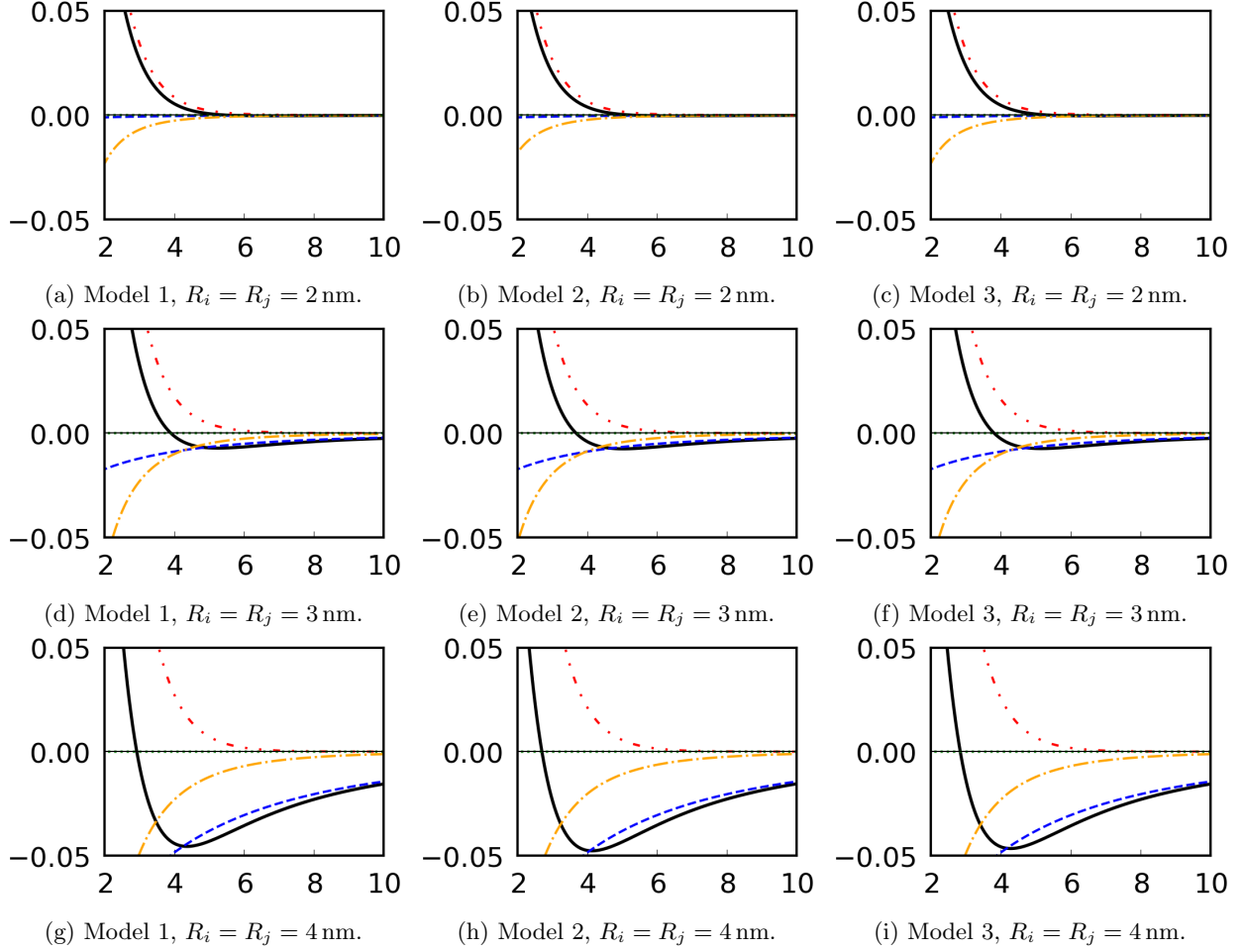


Figure S3: Interaction energy of two nanoparticles with equal radii in dependence on their intersurface distance, in the long range (2 nm to 10 nm), for the models 1, 2 and 3, from left to right. Other nanoparticle parameters are as shown in the article appendices.

Secondary minima

Figure S4 shows heatmaps of the secondary equilibrium positions for some combinations of values for the radii of the interacting particles (R_i and R_j). Wider variations are found in the larger particle rows, which shows that the radius of the smaller particle of the pair has a more determinant role. The differences between the models are not very marked visually, thus we also show some percentual variations between the models' results (Figure S5).

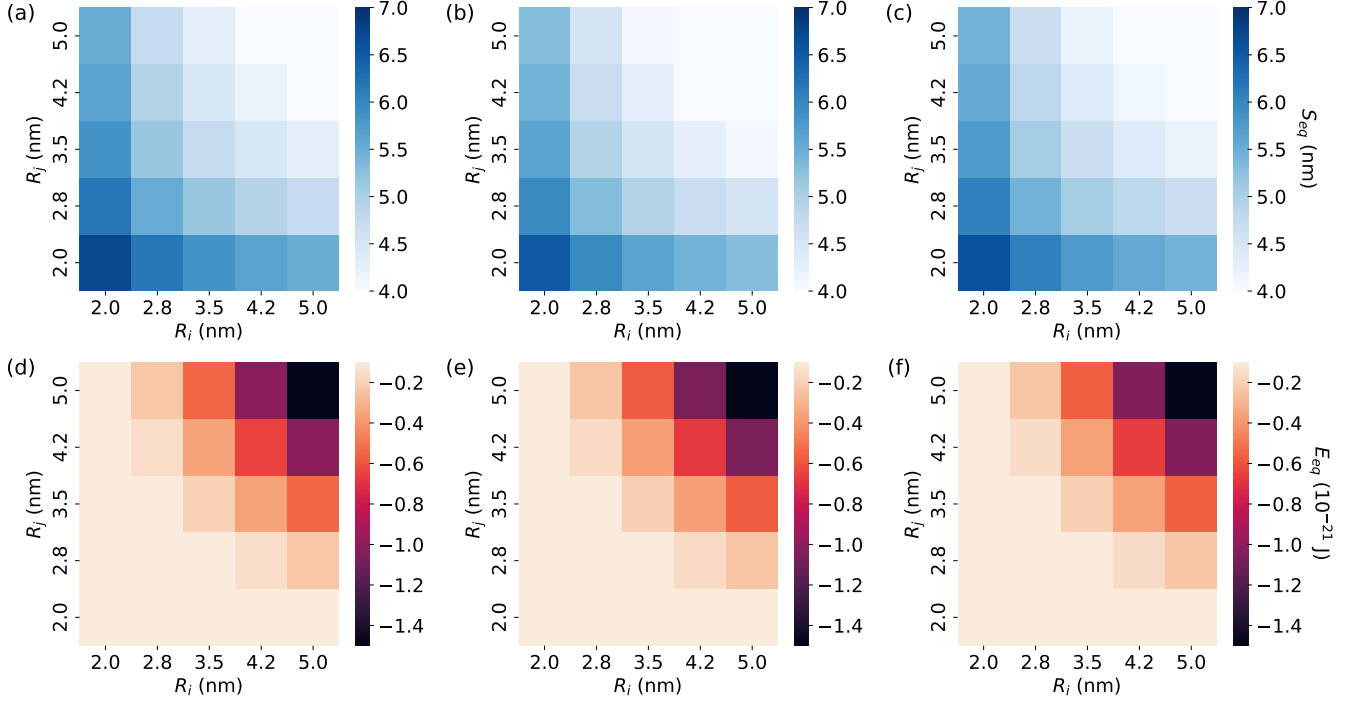


Figure S4: Heatmaps of the secondary equilibrium positions for Models 1 (a), 2 (b), and 3 (c). Below, corresponding heatmaps showing the secondary minima energy for Models 1 (d), 2 (e), and 3 (f) are presented.

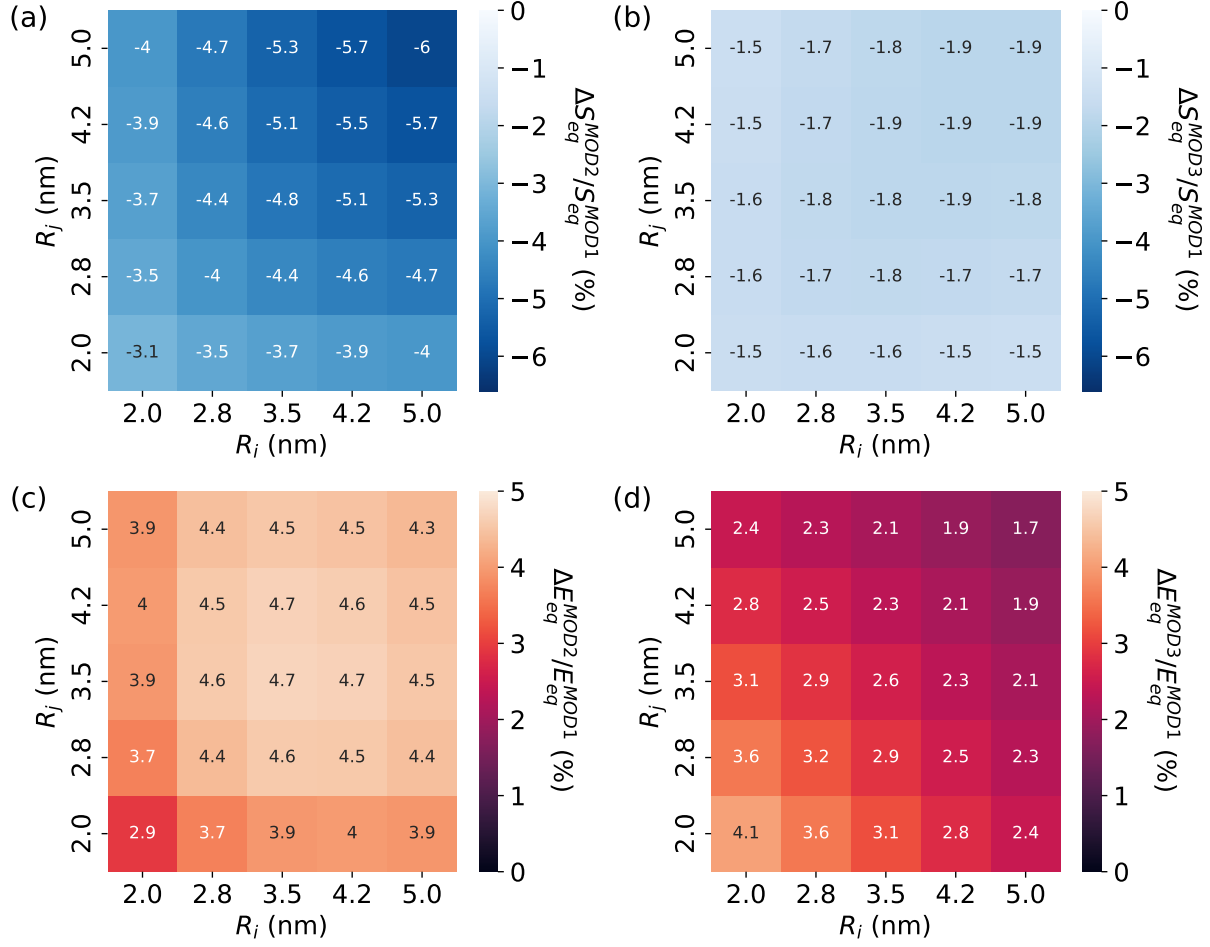


Figure S5: Heatmap showing the percentage difference in the secondary equilibrium distance between Models 2/1 (a) and Models 3/1 (b). The percentage difference in the corresponding energy depth is presented for Models 2/1 (c) and Models 3/1 (d).